A Three-stage Approach for Segmenting Degraded Color Images: Smoothing, Lifting and Thresholding (SLaT)

Xiaohao Cai, Raymond Chan, Mila Nikolova, *Seinor Member, IEEE,* and Tieyong Zeng

arXiv:1506.00060v1 [cs.CV] 30 May 2015

Abstract

In this paper, we propose a SLaT (Smoothing, Lifting and Thresholding) method with three stages for multiphase segmentation of color images corrupted by different degradations: noise, information loss, and blur. At the first stage, a convex variant of the Mumford-Shah model is applied to each channel to obtain a smooth image. We show that the model has unique solution under the different degradations. In order to properly handle the color information, the second stage is dimension lifting where we consider a new vector-valued image composed of the restored image and its transform in the secondary color space with additional information. This ensures that even if the first color space has highly correlated channels, we can still have enough information to give good segmentation results. In the last stage, we apply multichannel thresholding to the combined vector-valued image to find the segmentation. The number of phases is only required in the last stage, so users can choose or change it all without the need of solving the previous stages again. Experiments demonstrate that our SLaT method gives excellent results in terms of segmentation quality and CPU time in comparison with other state-of-the-art segmentation methods.

Index Terms

Mumford-Shah model, convex variational models, multiphase color image segmentation, color spaces.

I. Introduction

IMAGE segmentation is a fundamental and challenging task in image processing and computer vision. It can serve as a preliminary step for object recognition and interpretation, to mention a few. The goal of image segmentation is to group parts of the given image with similar characteristics together. These characteristics include, for example, edges, intensities, colors, and textures. For a human observer, image segmentation seems obvious, but consensus between different observers is seldom found. The problem is much more difficult to be solved by a computer. A nice overview of region-based and edge-based segmentation methods is given in [18]. In our work we investigate the image segmentation problem for color images corrupted by different types of degradations: noise, information loss and blur.

X. Cai is with the Department of Plant Sciences, and Department of Applied Mathematics and Theoretical Physics (DAMTP), University of Cambridge, CB2 3EA, Cambridge, UK. His work is partially supported by Welcome Trust and KAUST Award No. KUK-I1-007-43. Email: xc274@cam.ac.uk.

R. Chan is with the Department of Mathematics, The Chinese University of Hong Kong, Shatin, Hong Kong. His work is partially supported by HKRGC GRF Grant No. CUHK400412, CUHK300614, CRF Grant No. CUHK2/CRF/11G, AoE Grant AoE/M-05/12, CUHK DAG No. 4053007, and FIS Grant No. 1907303. Email: rchan@math.cuhk.edu.hk.

M. Nikolova is with the CNRS, ENS Cachan, 61 Avenue du President Wilson, F-94230 Cachan, France. Her work is partially supported by HKRGC GRF Grant No. CUHK300614. Email: nikolova@cmla.ens-cachan.fr.

T. Zeng is with the Department of Mathematics, Hong Kong Baptist University, Kowloon Tong, Hong Kong. His work is partially supported by NSFC 11271049, RGC 211911, 12302714 and RFGs of HKBU. Email: zeng@hkbu.edu.hk.

Let $\Omega \subset \mathbb{R}^2$ be a bounded open connected set, and $f : \Omega \to \mathbb{R}^d$ with $d \geq 1$ be a given vector-valued image. For example, $d = 1$ for gray-scale images and $d = 3$ for the usual RGB (red-green-blue) color images. One has $d > 3$ in many cases such as in hyperspectral imaging [38] or in medical imaging [46]. In this paper, we are mainly concerned with color images (i.e. $d = 3$) though our approach can be extended to higher-dimensional vector-valued images. Without loss of generality, we restrict the range of f to $[0, 1]^3$ and hence $f \in L^\infty(\Omega)$.

In literature, various studies have been carried out and many techniques have been considered for image segmentation [1], [15], [24], [30], [31], [43]–[45], [50]. For gray-scale images, i.e. $d = 1$, Mumford and Shah proposed in [34], [35] an energy minimization problem for image segmentation which finds optimal piecewise smooth approximations. More precisely, this problem was formulated in [35] as

$$E_{\mathrm{MS}}(g, \Gamma) := \frac{\lambda}{2} \int_\Omega (f - g)^2 dx + \frac{\mu}{2} \int_{\Omega \setminus \Gamma} |\nabla g|^2 dx + \mathrm{Length}(\Gamma), \tag{1}$$

where λ and μ are positive parameters, and $g : \Omega \to \mathbb{R}$ is continuous in $\Omega \setminus \Gamma$ but may be discontinuous across the sought-after boundary Γ. Here, the length of Γ can be written as $\mathcal{H}^1(\Gamma)$, the 1-dimensional Hausdorff measure in $\mathbb{R}^2$. Model (1) has attractive properties even though finding a globally optimal solution remains an open problem and it is an active area of research. A recent overview can be found in [3].

For image segmentation, the Chan-Vese model [15] pioneered a simplification of functional (1) where Γ partitions the image domain into two constant segments and thus $\nabla g = 0$ on $\Omega \setminus \Gamma$. More generally, for K constant regions Ω_i, $i \in \{1, \ldots, K\}$, the multiphase piecewise constant Mumford-Shah model [48] reads as

$$E_{\mathrm{PCMS}}\left(\{\Omega_i, c_i\}_{i=1}^K\right) = \frac{\lambda}{2} \sum_{i=1}^K \int_{\Omega_i} (f - c_i)^2 dx + \frac{1}{2} \sum_{i=1}^K \mathrm{Per}(\Omega_i), \tag{2}$$

where $\mathrm{Per}(\Omega_i)$ is the perimeter of Ω_i in Ω, all Ω_i's are pairwise disjoint and $\Omega = \bigcup_{i=1}^K \Omega_i$. The Chan-Vese model where $K = 2$ in (2) has many applications for two-phase image segmentation. Model (2) is a nonconvex problem, so the obtained solutions are in general local minimizers. To overcome the problem, convex relaxation approaches [6], [11], [13], [39], graph cut method [25] and fuzzy membership functions [31] were proposed.

After [15], many approaches decompose the segmentation process into several steps and here we give a brief overview of recent work in this direction. The paper [29] performs a simultaneous segmentation of the input image into arbitrarily many pieces using a modified version of model (1) and the final segmented image results from a stopping rule using a multigrid approach. In [17], an initial hierarchy of regions is obtained by greedy iterative region merging using model (2); the final segmentation is obtained by thresholding this hierarchy using hypothesis testing. The paper [2] first determines homogeneous regions in the noisy image with a special emphasis on topological changes; then each region is restored using model (1). Further multistage methods extending model (2) can be found in [47] where wavelet frames were used, and in [9] which is based on iterative thresholding of the minimizer of the ROF functional [42], just to cite a few. In the discrete setting, the piecewise constant Mumford-Shah model (2) amounts to the classical Potts model [40]. The use of this kind of functionals for image segmentation was pioneered by Geman and Geman in [22]. In [44], a coupled Potts model is used for direct partitioning of images using a convergent minimization scheme.

In [8], a conceptually different two-stage method for the segmentation of gray-scale images was proposed. In the first stage, a smoothed solution g is extracted from the given image f by

minimizing a non-tight convexification of the Mumford-Shah model (1). The segmented image is obtained in the second stage by applying a thresholding technique to g. This approach was extended in [12] to images corrupted by Poisson and Gamma noises. Since the basic concept of our method in this paper is similar, we will give more details on [8], [12] in Section II.

Extending or conceiving segmentation methods for color images is not a simple task since one needs to discriminate segments with respect to both luminance and chrominance information. The two-phase Chan-Vese model [15] was generalized to deal with vector-valued images in [14] by combining the information in the different channels using the data fidelity term. Many methods are applied in the usual RGB color space [7], [14], [18], [27], [29], [39], [44], among others. It is often mentioned that the RGB color space is not well adapted to segmentation because for real-world images the R, G and B channels can be highly correlated. In [41], RGB images are transformed into HSI (hue, saturation, and intensity) color space in order to perform segmentation. In [2] a general segmentation approach is developed for gray-value images and further extended to color images in the RGB, the HSV (hue, saturation, and value) and the CB (chromaticity-brightness) color spaces. However, a study on this point in [37] shows that the Lab (perceived lightness, red-green and yellow-blue) color space defined by the CIE (Commission Internationale de l'Eclairage) is better adapted for color image segmentation than the RGB and the HSI color spaces. In [17] RGB input images are first converted to Lab space. In [49] color features are described using the Lab color space and texture using histograms in RGB space.

A careful examination of the methods that transform a given RGB image to another color space (HSI, CB, Lab, ...) before performing the segmentation task shows that these algorithms are always applied only to noise-free RGB images (though these images unavoidably contain quantization and compression noise). For instance, this is the case of [2], [17], [41], [49], among others. One of the main reasons is that if the input RGB image is degraded, the degradation would be hard to control after a transformation to another color space [37].

Our goal is to develop an image segmentation method that has the following properties:

(a) work on vector-valued (color) images possibly corrupted with noise, blur and missing data;
(b) initialization independent and non-supervised (the number of segments is not fixed in advance);
(c) avoid dealing with nonconvex and combinatorial methods for the sake of stability;
(d) no need to solve the whole problem again when the number of segments required is changed;
(e) take into account perceptual edges between colors and between intensities so as to detect vector-valued objects with edges and also objects without edges.

Contributions. The main contribution of this paper is to propose a segmentation method having all these properties. Goals (a)–(d) lead us to explore possible extensions of the methods [8], [12] to vector-valued (color) images. Goal (e) requires finding a way to use information from perceptual color spaces even though our input images are corrupted; see goal (a). Let $\mathcal{V}_1$ and $\mathcal{V}_2$ be two color spaces. Our method has the following 3 steps:

1) Let the given degraded image be in $\mathcal{V}_1$. The convex variational model [8], [12] is applied in parallel to each channel of $\mathcal{V}_1$. This yields a restored smooth image. We show that the model has unique solution.
2) The second stage consists of color dimension lifting: we transform the smooth color image obtained at Stage 1 to a secondary color space $\mathcal{V}_2$ that provides us with complementary information. Then we combine these images as a new vector-valued image composed of all the channels from color spaces $\mathcal{V}_1$ and $\mathcal{V}_2$.
3) According to the desired number of phases K, we apply a multichannel thresholding to the combined $\mathcal{V}_1$-$\mathcal{V}_2$ image to obtain a segmented image.

We call our method "SLaT" for Smoothing, Lifting and Thresholding. Unlike the methods that perform segmentation in a different color space like [2], [17], [33], [41], [49], we can deal with degraded images thanks to Stage 1 which yields a smooth image that we can transform to another color space. We will fix $\mathcal{V}_1$ to be the RGB color space since one usually has RGB color images. We use the Lab color space [21] as the secondary color space $\mathcal{V}_2$ since it is often recommended for color segmentation [17], [18], [37]. The crucial importance of the dimension lifting Stage 2 is illustrated in Fig. 1 which shows the results without Stage 2, i.e. $\mathcal{V}_2 = \emptyset$ (middle) or with Stage 2 (right). To the best of our knowledge, it is the first time that two color spaces are used jointly in variational methods for segmentation. This provides us with additional information on the color



(a) Given noisy image (b) Using only RGB space (c) Using RGB+Lab space

Fig. 1. Segmentation results for a noisy image (a) without the dimension lifting in Stage 2 (b) and with Stage 2 (c).

image so that in all cases we can obtain very good segmentation results. The number of phases K is needed only in Stage 3. Its value can reasonably be selected based on the RGB image obtained at Stage 1.

Extensive numerical tests on synthetic and real-world images have shown that our method outperforms state-of-the-art variational segmentation methods like [31], [39], [44] in terms of segmentation quality, speed and parallelism of the algorithm, and the ability to segment images corrupted by different kind of degradations.

Outline. In Section II, we briefly review the models in [8], [12]. Our SLaT segmentation method is presented in Section III. In Section IV, we provide experimental results on synthetic and real-world images. Conclusion remarks are given in Section V.

II. Review of the Two-stage Segmentation Methods in [8], [12]

The methods in [8], [12] for the segmentation of gray-scale images are motivated by the observation that one can obtain a good segmentation by properly thresholding a smooth approximation of the given image. Thus in their first stage, these methods solve a minimization problem of the form

$$\inf_{g \in W^{1,2}(\Omega)} \left\{ \frac{\lambda}{2} \int_\Omega \Phi(f,g)dx + \frac{\mu}{2} \int_\Omega |\nabla g|^2 dx + \int_\Omega |\nabla g| dx \right\}, \tag{3}$$

where $\Phi(f,g)$ is the data fidelity term, μ and λ are positive parameters. We note that the model (3) is a convex non-tight relaxation of the Mumford-Shah model in (1). Paper [8] considers $\Phi(f,g) = (f - \mathcal{A}g)^2$ where $\mathcal{A}$ is a given blurring operator; when f is degraded by Poisson or Gamma noise, the statistically justified choice $\Phi(f,g) = \mathcal{A}g - f\log(\mathcal{A}g)$ is used in [12]. Under a weak assumption, the functional in (3) has a unique minimizer, say $\bar{g}$, which is a smooth approximation of f. The second stage is to use the K-means algorithm [28] to determine the thresholds for segmentation.

These methods have important advantages: they can segment degraded images and the minimizer $\bar{g}$ is unique. Further, the segmentation stage being independent from the optimization problem (3), one can change the number of phases K without solving (3) again.

III. SLaT: Our Segmentation Method for Color Images

Let $f = (f_1, \ldots, f_d)$ be a given color image with channels $f_i : \Omega \to \mathbb{R}, i = 1, \cdots, d$. For f an RGB image, $d = 3$. This given image f is typically a blurred and noisy version of an original unknown image. It can also be incomplete: we denote by Ω_0^i the open nonempty subset of Ω where the given f_i is known for channel i. Our SLaT segmentation method consists of three stages described next.

A. First Stage: Recovery of a Smooth Image

First, we restore each channel f_i of f separately by minimizing the functional E below

$$E(g_i) = \frac{\lambda}{2} \int_\Omega \omega_i \cdot \Phi(f_i, g_i) dx + \frac{\mu}{2} \int_\Omega |\nabla g_i|^2 dx + \int_\Omega |\nabla g_i| dx, \quad i = 1, \ldots, d, \tag{4}$$

where $|\cdot|$ stands for Euclidian norm and $\omega_i(\cdot)$ is the characteristic function of Ω_0^i, i.e.

$$\omega_i(x) = \begin{cases} 1, & x \in \Omega_0^i, \\ 0, & x \in \Omega \setminus \Omega_0^i. \end{cases} \tag{5}$$

For Φ in (4) we consider the following options:

i) $\Phi(f, g) = (f - \mathcal{A}g)^2$, the usual choice;
ii) $\Phi(f, g) = \mathcal{A}g - f \log(\mathcal{A}g)$ if data are corrupted by Poisson noise.

The restoration step amounts to the first stage in [8], [12] in the simple case when $d = 1$ and $\Omega_0^1 = \Omega$. Theorem III.1 below proves the existence and the uniqueness of the minimizer of (4). In view of (4) and (5), we define the linear operator $(\omega_i \mathcal{A})$ by

$$(\omega_i \mathcal{A}) : u(x) \in L^2(\Omega) \mapsto \omega_i(x)(\mathcal{A}u)(x) \in L^2(\Omega). \tag{6}$$

Theorem III.1. *Let Ω be a bounded connected open subset of $\mathbb{R}^2$ with a Lipschitz boundary. Let $\mathcal{A} : L^2(\Omega) \to L^2(\Omega)$ be bounded and linear. For $i \in \{1, \ldots, d\}$, assume that $f_i \in L^2(\Omega)$ and that $\mathrm{Ker}(\omega_i \mathcal{A}) \bigcap \mathrm{Ker}(\nabla) = \{0\}$ where Ker stands for null-space. Then (4) with either $\Phi(f_i, g_i) = (f_i - \mathcal{A}g_i)^2$ or $\Phi(f_i, g_i) = \mathcal{A}g_i - f_i \log(\mathcal{A}g_i)$ has a unique minimizer $\bar{g}_i \in W^{1,2}(\Omega)$.*

The proof is outlined in Appendix I. The condition $\mathrm{Ker}(\omega_i \mathcal{A}) \bigcap \mathrm{Ker}(\nabla) = \{0\}$ is mild—it means that $\mathrm{Ker}(\omega_i \mathcal{A})$ does not contain constant images.

The discrete model. In the discrete setting, Ω is an array of pixels, say of size $M \times N$, and our model (4) reads as

$$E(g_i) = \frac{\lambda}{2} \Psi(f_i, g_i) + \frac{\mu}{2} \|\nabla g_i\|_F^2 + \|\nabla g_i\|_{2,1}, \quad i = 1, \ldots, d.$$

Here

$$\Psi(f_i, g_i) := \sum_{j \in \Omega} \left(\omega_i \cdot (f_i - \mathcal{A}g_i)^2\right)_j \text{ or } \Psi(f_i, g_i) := \sum_{j \in \Omega} \left(\omega_i \cdot \left(\mathcal{A}g_i - f_i \log(\mathcal{A}g_i)\right)\right)_j.$$

The operator $\nabla = (\nabla_x, \nabla_y)$ is discretized using backward differences with Neumann boundary conditions. Further, $\|\cdot\|_F^2$ is the Frobenius norm, so

$$\|\nabla g_i\|_F^2 = \sum_{j \in \Omega} \left((\nabla_x g_i)_j^2 + (\nabla_y g_i)_j^2\right),$$

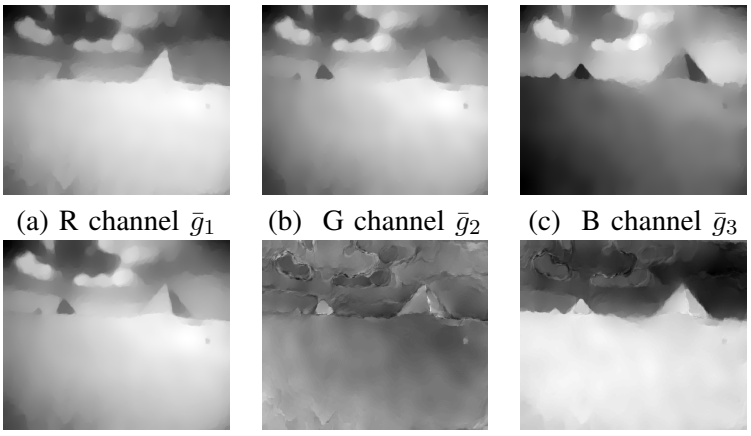
and $\|\nabla g_i\|_{2,1}$ is the usual discretization of the TV semi-norm given by

$$\|\nabla g_i\|_{2,1} = \sum_{j\in\Omega} \sqrt{(\nabla_x g_i)_j^2 + (\nabla_y g_i)_j^2}.$$

For each i, the minimizer $\bar{g}_i$ can be computed easily using different methods, for example the primal-dual algorithm [10], [16], alternating direction method with multipliers (ADMM) [5], or the split-Bregman algorithm [23]. Then we rescale each $\bar{g}_i$ onto $[0,1]$ to obtain $\{\bar{g}_i\}_{i=1}^d \in [0,1]^d$.

B. Second Stage: Dimension Lifting with Secondary Color Space

For the ease of presentation, in the following, we assume $\mathcal{V}_1$ is the RGB color space. The goal in color segmentation is to recover segments both in the luminance and in the chromaticity of the image. It is well known that the R, G and B channels can be highly correlated. For instance, the R, G and B channels of the output of Stage 1 for the noisy pyramid image in Fig. 1 are depicted in Fig. 2 (a)–(c). One can hardly expect to make a meaningful segmentation based on these channels—see the result in Fig. 1 (b), as well as Fig. 8 where other contemporary methods are compared.



(a) R channel $\bar{g}_1$ (b) G channel $\bar{g}_2$ (c) B channel $\bar{g}_3$

(d) L channel $\bar{g}_1^t$ (e) a channel $\bar{g}_2^t$ (f) b channel $\bar{g}_3^t$

Fig. 2. Channels comparison for the restored (smoothed) $\bar{g}$ in Stage 1 used in Fig. 1. (a)–(c): the R, G and B channels of $\bar{g}$; (d)–(f): the L, a and b channels of $\bar{g}^t$ – the Lab transform of $\bar{g}$. Both $\bar{g}$ and $\bar{g}^t$ were used to obtain the result in Fig. 1 (c).

Stage 1 provides us with a restored smooth image $\bar{g}$. In Stage 2, we perform dimension lifting in order to acquire additional information on $\bar{g}$ from a different color space that will help the segmentation in Stage 3. The choice is delicate. Popular choices of less-correlated color spaces include HSV, HSI, CB and Lab, as described in the Introduction. The Lab color space was created by the CIE with the aim to be perceptually uniform [21] in the sense that the numerical difference between two colors is proportional to perceived color difference. This is an important property for color image segmentation, see e.g. [17], [18], [37]. For this reason in the following we use the Lab as the additional color space. Here the L channel correlates to perceived lightness, while the a and b channels correlate approximately with red-green and yellow-blue, respectively. As an example we show in Fig. 2 (d)–(f) the L, a and b channels of the smooth $\bar{g}$ in Stage 1 for the noisy pyramid in Fig. 1 (a). The result in Fig. 1 (c) have shown that this additional color space helps the segmentation significantly.

Let $\bar{g}'$ denote Lab transform of $\bar{g}$. In order to compare $\bar{g}'$ with $\bar{g} \in [0,1]^3$, we rescale on [0,1] the channels of $\bar{g}'$ which yields an image denoted by $\bar{g}^t \in [0,1]^3$. By stacking together $\bar{g}$ and $\bar{g}^t$ we obtain a new vector-valued image $\bar{g}^*$ with $2d = 6$ channels:

$$\bar{g}^* := (\bar{g}_1, \bar{g}_2, \bar{g}_3, \bar{g}_1^t, \bar{g}_2^t, \bar{g}_3^t).$$

Our segmentation in Stage 3 is done on this $\bar{g}^*$.

C. Third Stage: Thresholding

Given the vector-valued image $\bar{g}^* \in [0,1]^{2d}$ for $d = 3$ from Stage 2 we want now to segment it into K segments. Here we design a properly adapted strategy to partition vector-valued images into K segments. It is based on the K-means algorithm [28] because of its simplicity and good asymptotic properties. According to the value of K, the algorithm clusters all points of $\{\bar{g}^*(x) \ : \ x \in \Omega\}$ into K Voronoi-shaped cells, say $\Sigma_1 \cup \Sigma_2 \cdots \cup \Sigma_K = \Omega$. Then we compute the mean vector $c_k \in \mathbb{R}^6$ on each cell Σ_k by

$$c_k = \frac{\int_{\Sigma_k} \bar{g}^* dx}{\int_{\Sigma_k} dx}, \quad k = 1, \ldots, K. \tag{7}$$

We recall that each entry $c_k[i]$ for $i = 1, \cdots, 6$ is a value belonging to $\{\mathrm{R}, \mathrm{G}, \mathrm{B}, \mathrm{L}, \mathrm{a}, \mathrm{b}\}$, respectively. Using $\{c_k\}_{k=1}^K$, we separate $\bar{g}^*$ into K phases by

$$\Omega_k := \Big\{ x \in \Omega \ : \ \|\bar{g}^*(x) - c_k\|_2 = \min_{1 \le j \le K} \|\bar{g}^*(x) - c_j\|_2 \Big\}, \quad k = 1, \ldots, K. \tag{8}$$

It is easy to verify that $\{\Omega_k\}_{k=1}^K$ are disjoint and that $\bigcup_{k=1}^K \Omega_k = \Omega$. The use of the ℓ_2 distance here follows from our model (4) as well as from the properties of the Lab color space [17], [21]. Note that in the simple case when $c_k \in \mathbb{R}$ (i.e., $d = 1$), the thresholding scheme (8) reduces to the one used in [8], [12].

D. The SLaT Algorithm

We summarize our 3-stage segmentation method for color images in Algorithm 1. Like the Mumford-Shah model, our model (4) has two parameters λ and μ. Extensive numerical tests have shown that we can fix $\mu = 1$. We choose λ empirically; the method is quite stable with respect to this choice.

Algorithm 1: Three-stage Segmentation Method (SLaT) for Color Images

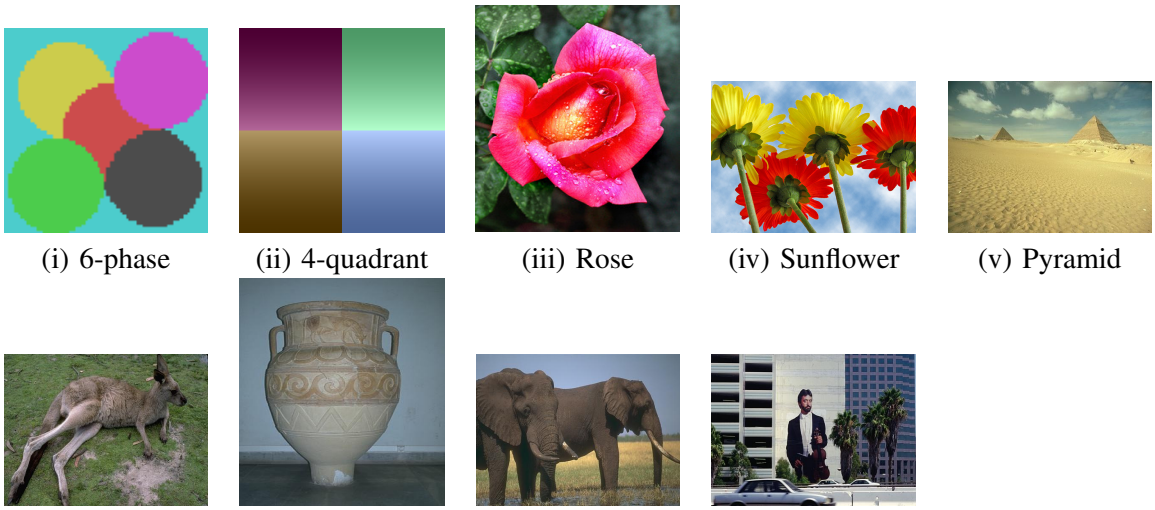
Input: Given color image $f \in \mathcal{V}_1$ and color space $\mathcal{V}_2$.
Output: Phases $\Omega_k, k = 1, \ldots, K$.

1 Stage one: compute $\bar{g}_i$ the minimizer in (4), rescale it on $[0,1]$ for $i = 1, 2, 3$ and set $\bar{g} = (\bar{g}_1, \bar{g}_2, \bar{g}_3)$ in $\mathcal{V}_1$;
2 Stage two:
3 compute $\bar{g}' \in \mathcal{V}_2$, the transform of $\bar{g}$ in $\mathcal{V}_2$, to obtain $\bar{g}^t = (\bar{g}_1^t, \bar{g}_2^t, \bar{g}_3^t)$;
4 form $\bar{g}^* = (\bar{g}_1, \bar{g}_2, \bar{g}_3, \bar{g}_1^t, \bar{g}_2^t, \bar{g}_3^t)$;
5 Stage three:
6 choose K, apply the K-means algorithm to obtain $\{c_k\}_{k=1}^K$ in (7) and find the segments $\Omega_k, k = 1, \ldots, K$ using (8).

We emphasize that our method is quite suitable for parallelism since $\{\bar{g}_i\}_{i=1}^3$ in Stage 1 can be computed in parallel.

IV. Experimental Results

In this section, we compare our SLaT method with three state-of-the-art variational color segmentation methods [31], [39], [44]. Method [31] uses fuzzy membership functions to approximate the piecewise constant Mumford-Shah model (2). Method [39] uses a primal-dual algorithm to solve a convex relax model of (2) with a fixed code book. Method [44] uses an ADMM algorithm to solve the model (2) (without phase number K) with Potts priors. The codes we used are provided by the authors, and the parameters in the codes were chosen by trial and error to give the best results of each method. For our model (4), we fix $\mu = 1$ and only vary λ. In the segmented figures below, each phase is represented by the average intensity of that phase in the image. All the results were tested on a MacBook with 2.4 GHz processor and 4GB RAM, and MATLAB R2014a.



(i) 6-phase (ii) 4-quadrant (iii) Rose (iv) Sunflower (v) Pyramid

(vi) Kangaroo (vii) Vase (viii) Elephant (ix) Man

Fig. 3. Images used in our tests.

We present the tests on two synthesis and seven real-world images given in Fig. 3. The images are all in RGB color space. We considered combinations of three different forms of image degradation: noise, information loss, and blur. The Gaussian and Poisson noisy images are all generated using MATLAB function `imnoise`. For Gaussian noisy images, the Gaussian noise we added are all of mean 0 and variance 0.001 or 0.1. To apply the Poisson noise, we linearly stretch the given image f to [1, 255] first, then linearly stretch the noisy image back to [0, 1] for testing. The mean of the Poisson distribution is 10. For information loss case, we deleted 60% pixels values randomly. The blur in the test images were all obtained by a vertical motion-blur with 10 pixels length.

In Stage 1 of our method, the primal-dual algorithm [10], [16] and the split-Bregman algorithm [23] are adopted to solve (4) for $\Phi(f, g) = \mathcal{A}g - f\log(\mathcal{A}g)$ and $\Phi(f, g) = (f - \mathcal{A}g)^2$, respectively. We terminate the iterations when $\frac{\|g_i^{(k)} - g_i^{(k+1)}\|_2}{\|g_i^{(k+1)}\|_2} < 10^{-4}$ for $i = 1, 2, 3$ or when the maximum iteration number 200 is reached. In Stage 2, the transformation from RGB to Lab color spaces is implemented by MATLAB build-in function `makecform('srgb2lab')`. In Stage 3, given the user defined number of phases K, the thresholds are determined automatically by MATLAB K-means function `kmeans`. Since $\bar{g}^*$ is calculated prior to the choice of K, users can try different K and segment the image all without re-computing $\bar{g}^*$.

A. Segmentation of Synthetic Images

Example 1. Six-phase segmentation. Fig. 4 gives the result on a six-phase synthetic image containing five overlapping circles with different colors. The image is corrupted by Gaussian noise, information loss, and blur, see Fig. 4 (A), (B), and (C) respectively. From the figures, we see that method Li *et al.* [31] and method Storath *et al.* [44] both fail for the three experiments while method Pock *et al.* [39] fails for the case of information lost.

Table I shows the segmentation accuracy by giving the ratio of the number of correctly segmented pixels to the total number of pixels. The best ratios are printed in bold face. From the table, we see that our method gives the highest accuracy for the case of information loss and blur. For denoising, method [39] is 0.02% better. Table II gives the iteration numbers of each method and the CPU time cost. We see that our method outperforms the others compared. Moreover, if using parallel technique, the time can be reduced roughly by a factor of 3.

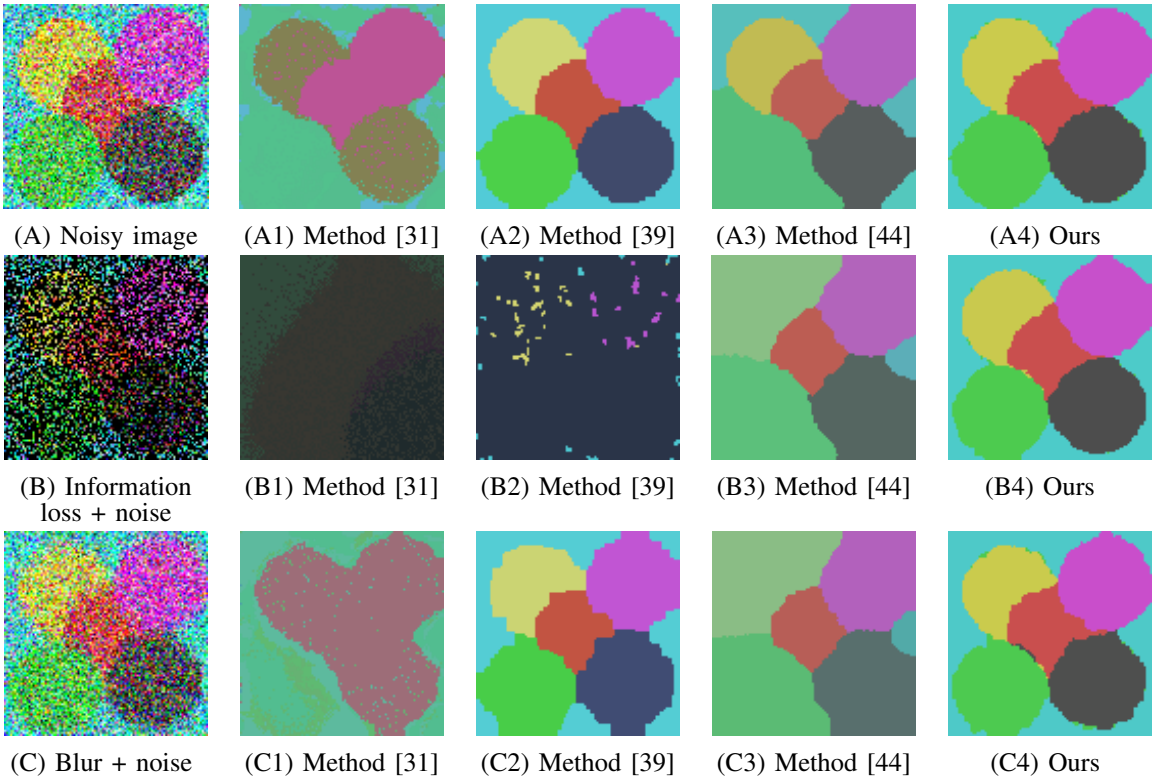


Fig. 4. Six-phase synthetic image segmentation (size: 100×100). (A): Given Gaussian noisy image with mean 0 and variance 0.1; (B): Given Gaussian noisy image with 60% information loss; (C): Given blurry image with Gaussian noise; (A1–A4), (B1–B4) and (C1–C4): Results of methods [31], [39], [44], and our SLaT on (A), (B) and (C), respectively.

Example 2. Four-phase segmentation. Our next test is on a four-phase synthetic image containing four rectangles with different colors, see Fig. 5. The variable illumination in the figure make the segmentation very challenging. The results shows that in all cases (noise, information loss and blur) all three competing methods [31], [39], [44] fail while our method gives extremely good results. Table II shows further that the time cost of our method is the least.

TABLE I
COMPARISON OF PERCENTAGE OF CORRECT PIXELS FOR THE 6-PHASE SYNTHETIC IMAGE.

		Method [31]	Method [39]	Method [44]	Our SLaT method
Fig. 4	(A)	70.11%	**99.53%**	82.55%	99.51%
	(B)	13.90%	16.92%	85.04%	**99.25%**
	(C)	28.08%	98.58%	74.77%	**98.88%**
Average		37.36%	71.68%	80.79%	**99.21%**

TABLE II
ITERATION NUMBERS AND CPU TIME IN SECONDS.

		Method [31]		Method [39]		Method [44]		Our SLaT method	
Fig.		iter.	time	iter.	time	iter.	time	iter. for $\{g_i\}_{i=1}^3$	time
4	(A)	200	5.03	150	6.02	20	4.40	(92, 86, 98)	**2.53**
	(B)	200	5.65	150	4.01	16	3.65	(98, 95, 106)	**2.73**
	(C)	200	6.54	150	4.03	17	4.18	(97, 95, 94)	**2.48**
5	(A)	200	13.92	150	13.89	17	16.89	(54, 54, 51)	**5.47**
	(B)	200	13.16	150	14.32	14	13.62	(101, 92, 88)	**7.74**
	(C)	200	17.68	150	16.37	16	15.75	(154, 147, 142)	**9.89**
6	(A)	200	10.58	150	7.53	19	11.62	(50, 73, 93)	**5.11**
	(B)	200	9.59	150	7.36	20	14.64	(84, 105, 115)	**6.43**
	(C)	200	10.39	150	**7.39**	19	9.76	(200, 200, 200)	17.75
7	(A)	200	44.26	150	66.01	19	106.35	(97, 106, 109)	**25.13**
	(B)	200	52.12	150	54.76	20	110.68	(148, 161, 171)	**38.30**
	(C)	200	44.51	150	55.09	18	101.09	(116, 125, 124)	**30.00**
8	(A)	200	17.76	150	**19.02**	16	25.08	(80, 83, 99)	20.99
	(B)	200	18.41	150	**16.45**	16	28.33	(109, 114, 129)	22.45
	(C)	200	18.02	150	**18.21**	15	31.93	(127, 120, 144)	30.92
9	(A)	200	18.47	150	19.62	15	27.56	(47, 42, 62)	**10.98**
	(B)	200	17.35	150	16.63	15	26.63	(86, 85, 93)	**15.93**
	(C)	200	18.07	150	17.61	15	23.13	(48, 48, 52)	**15.02**
10	(A)	200	24.57	150	31.64	20	56.28	(101, 95, 94)	**27.29**
	(B)	200	27.15	150	28.92	21	63.02	(154, 142, 131)	**27.89**
	(C)	200	26.54	150	**29.79**	20	55.45	(161, 147, 141)	33.79
11	(A)	200	26.62	150	32.87	17	87.13	(35, 35, 36)	**14.23**
	(B)	200	24.77	150	26.39	16	60.98	(102, 102, 103)	**18.99**
	(C)	200	25.26	150	31.16	18	77.73	(48, 50, 58)	**18.15**
12	(A)	200	32.23	150	41.91	19	47.12	(106, 102, 108)	**21.93**
	(B)	200	34.83	150	44.70	20	53.48	(116, 116, 117)	**23.95**
	(C)	200	35.01	150	49.93	19	49.14	(67, 65, 63)	**21.04**
Average		200	22.17	150	25.25	18	41.69	(99, 99, 104)	**17.67**

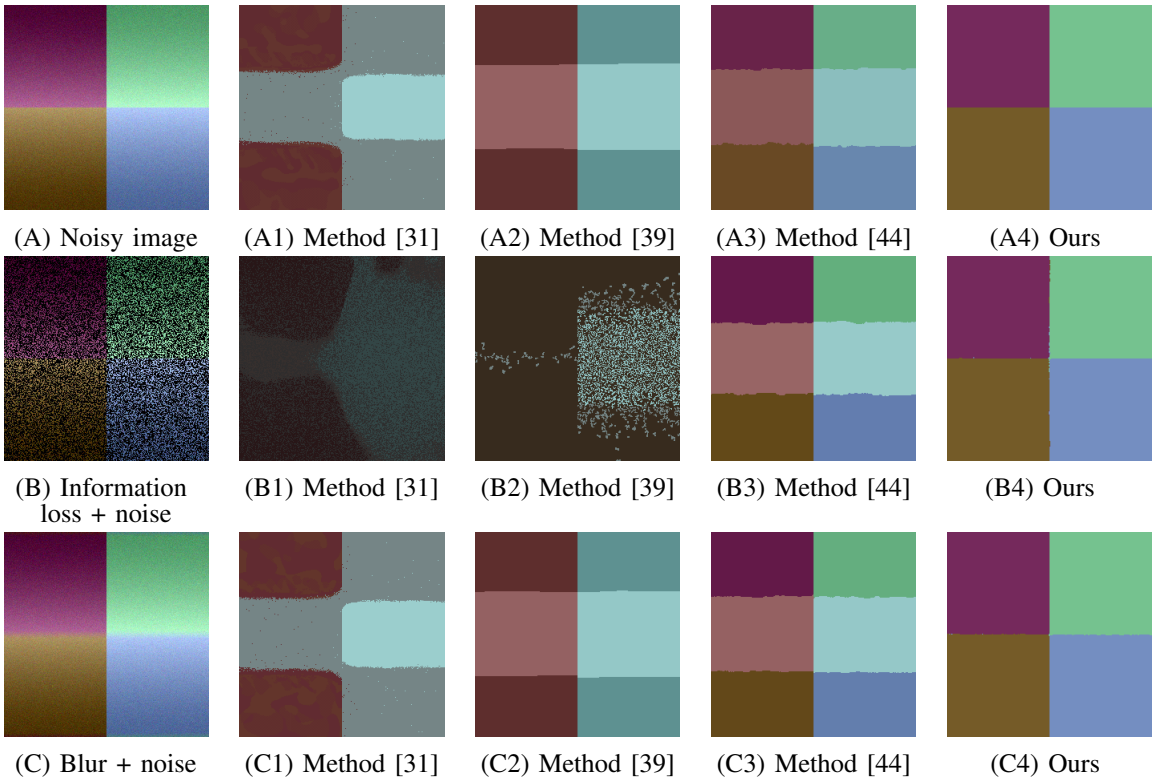


Fig. 5. Four-phase synthetic image segmentation (size: 256×256). (A): Given Gaussian noisy image with mean 0 and variance 0.001; (B): Given Gaussian noisy image with 60% information loss; (C): Given blurry image with Gaussian noise; (A1–A4), (B1–B4) and (C1–C4): Results of methods [31], [39], [44], and our SLaT on (A), (B) and (C), respectively.

B. Segmentation of Real-world Color Images

In this section, we compare our method with the three competing methods for 7 real-world color images in two-phase and multiphase segmentations, see Figs. 6–12. We see from the figures that our method is far superior than those by the competing methods. The timing of the methods given in Table II shows that our method in most of the cases gives the least timing. Again, we emphasize that our method is easily parallelizable. All presented experiments clearly show that all goals listed in Introduction are fulfilled.

V. Conclusions

In this paper we proposed a three-stage image segmentation method for color images. At the first stage of our method, a convex variational model is used in parallel on each channel of the color image to obtain a smooth color image. Then in the second stage we transform this smooth image to a secondary color space so as to obtain additional information of the image in the less-correlated color space. In the last stage, multichannel thresholding is used to threshold the combined image from the two color spaces. The new three-stage method, named SLaT for Smoothing, Lifting and Thresholding, has the ability to segment images corrupted by noise, blur, or when some pixel information is lost. Experimental results on RGB images coupled with Lab secondary color space demonstrate that our method gives much better segmentation results than some state-of-the-art segmentation models both in terms of quality and CPU time cost. Our future work includes finding

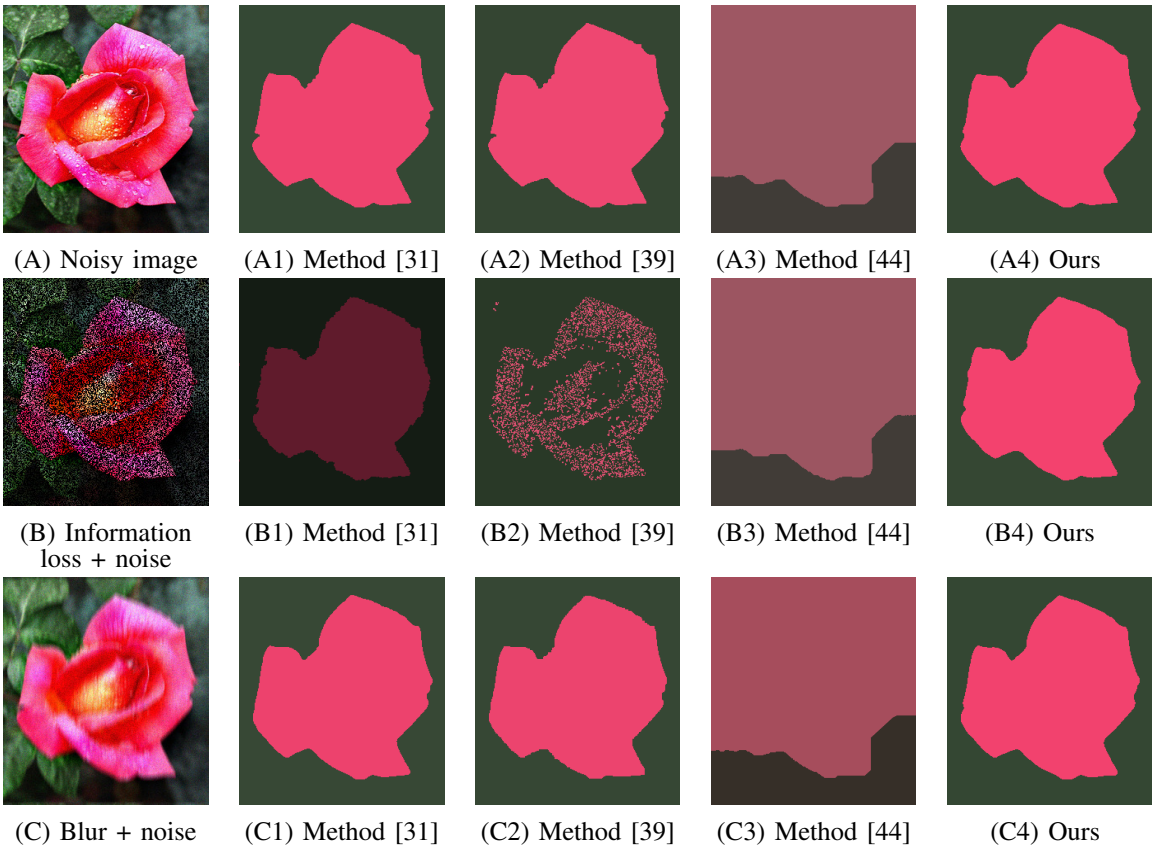


Fig. 6. Two-phase rose segmentation (size: 303×250). (A): Given Poisson noisy image; (B): Given Poisson noisy image with 60% information loss; (C): Given blurry image with Poisson noise; (A1-A4), (B1-B4) and (C1-C4): Results of methods [31], [39], [44], and our SLaT on (A), (B) and (C), respectively.

an automatical way to determine λ and possibly an improved model (4) that can better promote geometry.

ACKNOWLEDGMENT

The authors thank G. Steidl and M. Bertalmío for constructive discussions.

APPENDIX I: PROOF OF THEOREM III.1

First consider $\Phi(f_i, g_i) = (f_i - \mathcal{A}g_i)^2$. Using (6), $E(g_i)$ defined in (4) can be rewritten as

$$E(g_i) = \frac{\lambda}{2}\int_\Omega (\omega_i \cdot f_i - (\omega_i \mathcal{A})g_i)^2 dx + \frac{\mu}{2}\int_\Omega |\nabla g_i|^2 dx + \int_\Omega |\nabla g_i| dx.$$

Noticing that $\omega_i \cdot f_i \in L^2(\Omega)$ and that $(\omega_i \mathcal{A}) : L^2(\Omega) \to L^2(\Omega)$ is linear and bounded, the statement follows from [8, Theorem 2.4.].

Next consider that $\Phi(f_i, g_i) = \mathcal{A}g_i - f_i \log(\mathcal{A}g_i)$. Then

$$E(g_i) = \frac{\lambda}{2}\int_\Omega \omega_i \cdot (\mathcal{A}g_i) - (\omega_i \cdot f_i)\log(\mathcal{A}g_i) dx + \frac{\mu}{2}\|\nabla g_i\|^2_{L^2(\Omega)} + \|\nabla g_i\|_{L^2(\Omega)}.$$

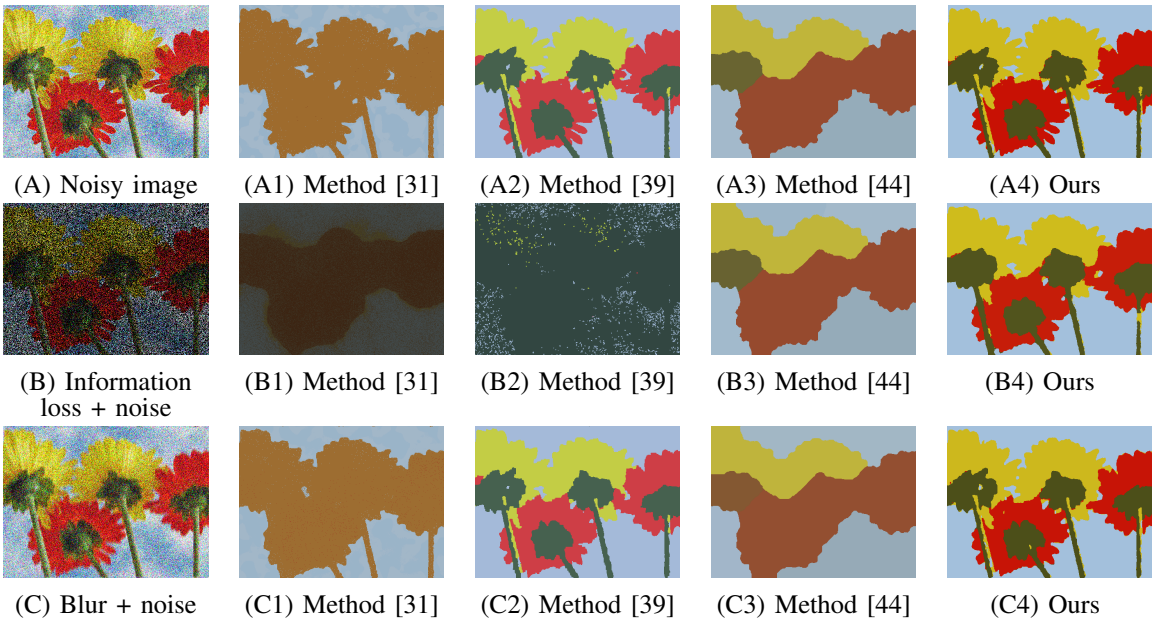


Fig. 7. Four-phase sunflower segmentation (size: 375×500). (A): Given Gaussian noisy image with mean 0 and variance 0.1; (B): Given Gaussian noisy image with 60% information loss; (C): Given blurry image with Gaussian noise; (A1-A4), (B1-B4) and (C1-C4): Results of methods [31], [39], [44], and our SLaT on (A), (B) and (C), respectively.

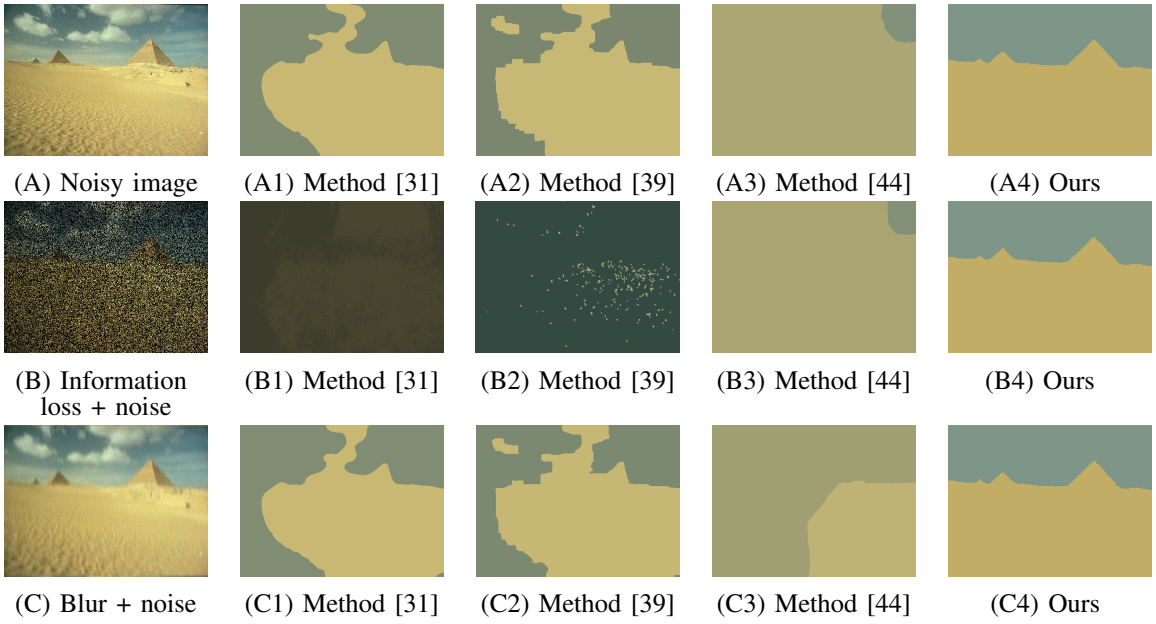


Fig. 8. Two-phase pyramid segmentation (size: 321×481). (A): Given Gaussian noisy image with mean 0 and variance 0.001; (B): Given Gaussian noisy image with 60% information loss; (C): Given blurry image with Gaussian noise; (A1-A4), (B1-B4) and (C1-C4): Results of methods [31], [39], [44], and our SLaT on (A), (B) and (C), respectively.

I) Existence: Since $W^{1,2}(\Omega)$ is a reflective Banach space and $E(g_i)$ is convex lower semi-continuous, by [19, Proposition 1.2] we need to prove that $E(g_i)$ is coercive on $W^{1,2}(\Omega)$, i.e. that $E(g_i) \to +\infty$ as $\|g_i\|_{W^{1,2}(\Omega)} := \|g_i\|_{L^2(\Omega)} + \|\nabla g_i\|_{L^2(\Omega)} \to +\infty$.

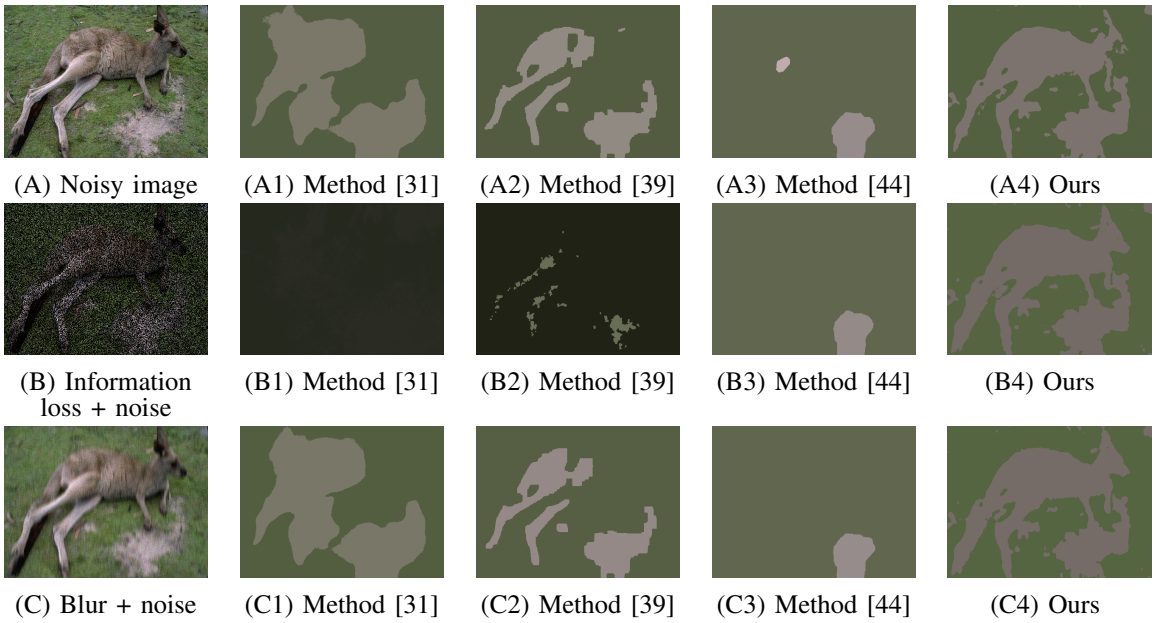


Fig. 9. Two-phase kangaroo segmentation (size: 321×481). (A): Given Poisson noisy image; (B): Given Poisson noisy image with 60% information loss; (C): Given blurry image with Poisson noise; (A1-A4), (B1-B4) and (C1-C4): Results of methods [31], [39], [44], and our SLaT on (A), (B) and (C), respectively.

The function $\mathcal{A}g_i \mapsto (\mathcal{A}g_i - f \log \mathcal{A}g_i)$ is strictly convex with a minimizer pointwisely satisfying $\mathcal{A}g_i = f \in [0,1]$, hence $\Phi(f_i, g_i) \geq 0$. Thus $\|\nabla g_i\|_{L^2(\Omega)}$ is upper bounded by $E(g_i) > 0$ for any $g_i \in W^{1,2}(\Omega)$ and $f \neq 0$. Using the Poincaré inequality, see [20], we have:

$$\|g_i - g_{i_\Omega}\|_{L^2(\Omega)} \leq C_1 \|\nabla g_i\|_{L^2(\Omega)} \leq C_1 E(g_i), \tag{9}$$

where $C_1 > 0$ is a constant and $g_{i_\Omega} = \frac{1}{|\Omega|} \int_\Omega g_i dx$. Let us set $C_2 := \left(1 - \frac{1}{e}\|f_i\|_\infty\right)$. We have $C_2 > 0$ because $\|f_i\|_\infty \leq 1$. Recall the fact that $\frac{t}{e} \geq \log t$ for any $t > 0$ which can be easily verified by showing that $t/e - \log t$ is convex for $t > 0$ with minimum at e. Hence we have

$$\omega_i \cdot \Phi(f_i, g_i) \geq (\omega_i \mathcal{A})\ g_i - \frac{1}{e}(\omega_i \cdot f_i)\mathcal{A}g_i = \omega_i \cdot (1 - \frac{1}{e} f_i)\mathcal{A}g_i \geq C_2\ (\omega_i \mathcal{A})\ g_i$$

which should be understood pointwisely. Hence,

$$\|(\omega_i \mathcal{A})\ g_i\|_{L^1(\Omega)} \leq \frac{2}{C_2 \lambda} E(g_i). \tag{10}$$

Let $C_3 := \|(\omega_i \mathcal{A})\mathbf{1}\|_{L^1(\Omega)}$ where $\mathbf{1}(x) = 1$ for any $x \in \Omega$. Using $\mathrm{Ker}(\nabla) = \{u \in L^2(\Omega) : u = c\ 1 \text{ a.e. for } x \in \Omega, c \in \mathbb{R}\}$ together with the assumption $\mathrm{Ker}(\omega_i \mathcal{A}) \bigcap \mathrm{Ker}(\nabla) = \{0\}$ one has $C_3 > 0$. Using (10) together with the fact that $g_{i_\Omega} > 0$ yields

$$|g_{i_\Omega}|\ \|(\omega_i \mathcal{A})\mathbf{1}\|_{L^1(\Omega)} = |g_{i_\Omega}|\ C_3 = \|\omega_i \cdot (\mathcal{A}\mathbf{1} g_{i_\Omega})\|_{L^1(\Omega)} \leq \frac{2}{C_2 \lambda} E(g_i),$$

and thus

$$|g_{i_\Omega}| \leq \frac{2}{C_2 C_3 \lambda} E(g_i).$$

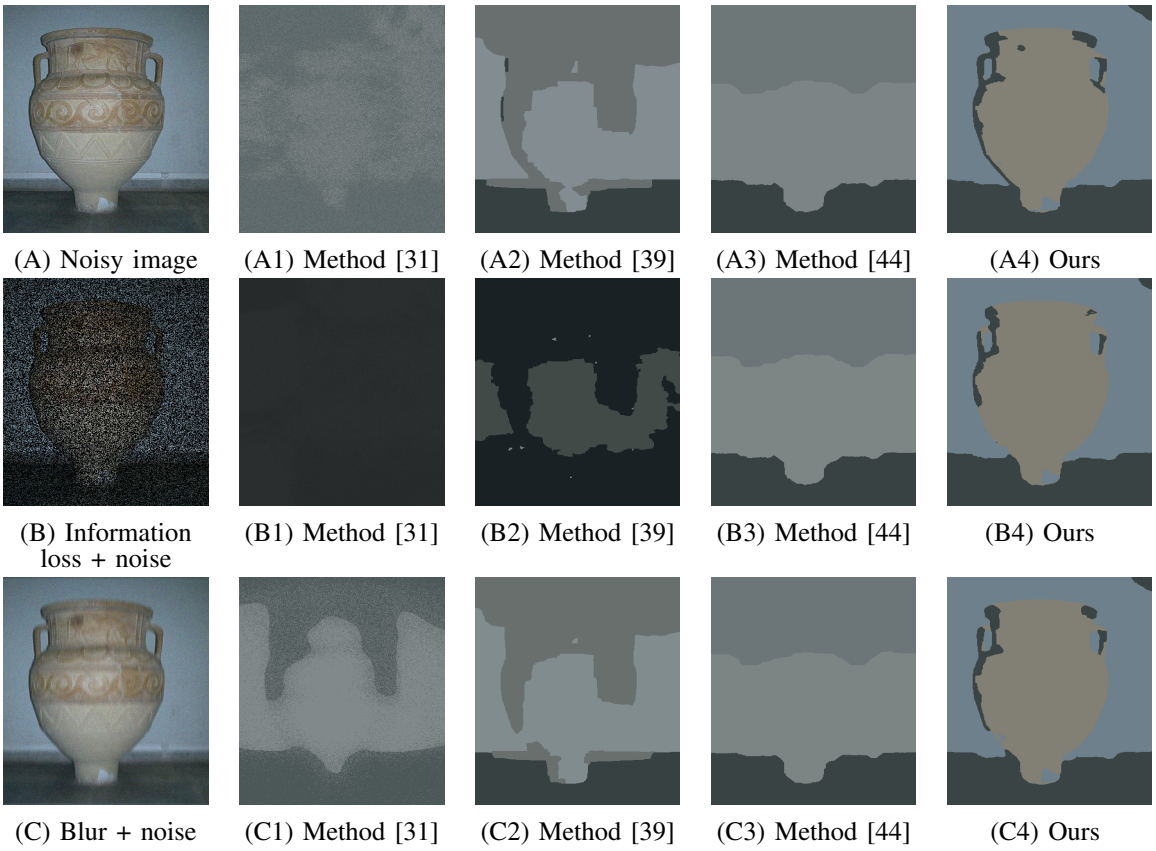


Fig. 10. Three-phase vase segmentation (size: 481×321). (A): Given Gaussian noisy image with mean 0 and noise 0.001; (B): Given Gaussian noisy image with 60% information loss; (C): Given blurry image with Gaussian noise; (A1-A4), (B1-B4) and (C1-C4): Results of methods [31], [39], [44], and our SLaT on (A), (B) and (C), respectively.

Applying the triangular inequality in (9) gives $\|g_i\|_{L^2(\Omega)} - |g_{i_\Omega}| \leq C_1 \|\nabla g_i\|_{L^2(\Omega)}$. Hence

$$\|g_i\|_{L^2(\Omega)} \leq |g_{i_\Omega}| + C_1 \|\nabla g_i\|_{L^2(\Omega)} \leq \left(\frac{2}{C_2 C_3 \lambda} + 1\right) E(g_i).$$

Comparing with (9) yet again shows that we have obtained

$$\|g_i\|_{W^{1,2}(\Omega)} = \|g_i\|_{L^2(\Omega)} + \|\nabla g_i\|_{L^2(\Omega)} \leq \left(\frac{2}{C_2 C_3 \lambda} + 1 + C_1\right) E(g_i).$$

Therefore, E is coercive.

II) Uniqueness: Suppose $\bar{g}_{i_1}$ and $\bar{g}_{i_2}$ are both minimizers of $E(g_i)$. The convexity of E and the strict convexity of $\mathcal{A}g_i \mapsto (\mathcal{A}g_i - f \log \mathcal{A}g_i)$ entail $\mathcal{A}\bar{g}_{i_1} = \mathcal{A}\bar{g}_{i_2}$ on Ω_0^i and $\nabla \bar{g}_{i_1} = \nabla \bar{g}_{i_2}$. Further, the assumption on $\mathrm{Ker}(\omega_i \mathcal{A}) \bigcap \mathrm{Ker}(\nabla)$ shows that $\bar{g}_{i_1} = \bar{g}_{i_2}$.

REFERENCES

[1] P. Arbelaez, M. Maire, C. Fowlkes and J. Malik. Contour detection and hierarchical image segmentation. *IEEE Transactions on Pattern Analysis and Machine Intelligence*, 33(5):898–916, 2011.

[2] H. Benninghoff and H. Garcke. Efficient Image Segmentation and Restoration Using Parametric Curve Evolution with Junctions and Topology Changes. *SIAM Journal on Imaging Sciences*, 7(3):1451–1483, 2014.

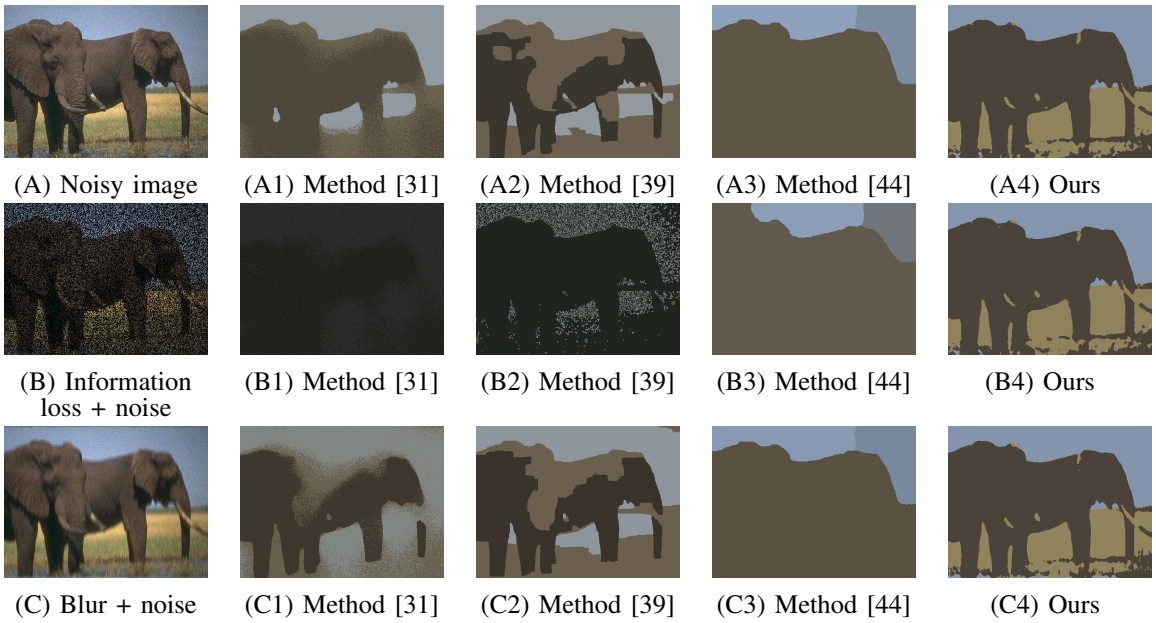


Fig. 11. Three-phase elephant segmentation (size: 321×481). (A): Given Poisson noisy image; (B): Given Poisson noisy image with 60% information loss; (C): Given blurry image with Poisson noise; (A1-A4), (B1-B4) and (C1-C4): Results of methods [31], [39], [44], and our SLaT on (A), (B) and (C), respectively.

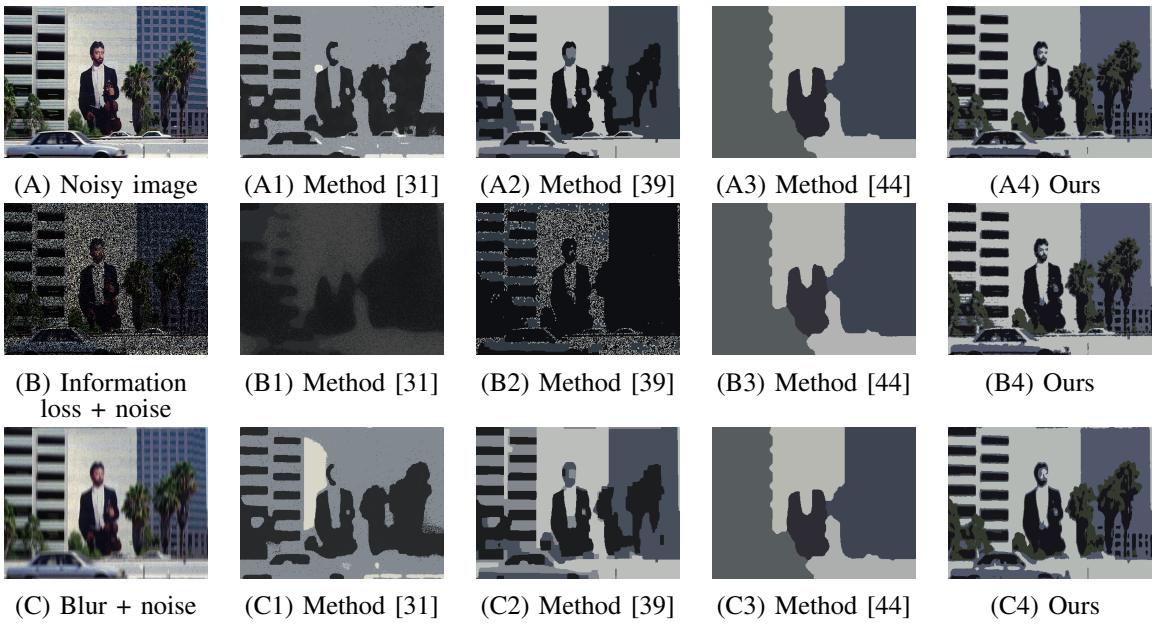


Fig. 12. Four-phase man segmentation (size: 321×481). (A): Given Poisson noisy image; (B): Given Poisson noisy image with 60% information loss; (C): Given blurry image with Poisson noise; (A1-A4), (B1-B4) and (C1-C4): Results of methods [31], [39], [44], and our SLaT on (A), (B) and (C), respectively.

[3] L. Bar, T. F. Chan, G. Chung, M. Jung, N. Kiryati, N. Sochen and L. A. Vese. Mumford and Shah Model and Its Applications to Image Segmentation and Image Restoration *Handbook of Mathematical Methods in Imaging*, 2nd edition, Editor: O. Scherzer, Springer 2015 (online).

[4] P. Blomgren and T. Chan. Color TV: Total Variation Methods for Restoration of Vector-Valued Images. *IEEE Transactions on Image Processing*, 7(3):304–309, 1998.

[5] S. Boyd, N. Parikh, E. Chu, B. Peleato, and J. Eckstein. Distributed optimization and statistical learning via the alternating direction method of multipliers. *Foundations and Trends in Machine Learning*, 3:1–122, 2010.

[6] X. Bresson, S. Esedoglu, P. Vandergheynst, J. Thiran, and S. Osher. Fast global minimization of the active contour/snake model. *Journal of Mathematical Imaging and Vision*, 28:151–167, 2007.

[7] X. Cai. Variational image segmentation model coupled with image restoration achievements. *Pattern Recognition*, 48:2029–2042, 2015.

[8] X. Cai, R. Chan, and T. Zeng. A two-stage image segmentation method using a convex variant of the Mumford-Shah model and thresholding. *SIAM Journal on Imaging Sciences*, 6(1):368–390, 2013.

[9] X. Cai and G. Steidl. Multiclass segmentation by iterated rof thresholding. In *EMMCVPR, LNCS, Springer*, pages 237–250, 2013.

[10] A. Chambolle and T. Pock. A first-order primal-dual algorithm for convex problems with applications to imaging. *Journal of Mathematical Imaging and Vision*, 40:120–145, 2011.

[11] A. CHAMBOLLE, D. CREMERS, AND T. POCK. *A convex approach to minimal partitions*, *SIAM Journal on Imaging Sciences*, 5(4), pp. 1113–1158 2012.

[12] R. Chan, H. Yang, and T. Zeng. A two-stage image segmentation method for blurry images with Poisson or multiplicative gamma noise. *SIAM Journal on Imaging Sciences*,7(1):98–127, 2014.

[13] T. Chan, S. Esedoglu, and M. Nikolova. Algorithms for finding global minimizers of image segmentation and denoising models. *SIAM Journal on Applied Mathematics*, 66:1632–1648, 2006.

[14] T. Chan, B. Sandberg, and L. Vese. Active contours without edges for vector-valued images. *Journal of Visual Communication and Image Representation*, 11:130–141, 2000.

[15] T. Chan and L. Vese. Active Contours Without Edges. *IEEE Transactions on Image Processing*, 10:266–277, 2001.

[16] Y. Chen, G. Lan, and Y. Ouyang. Optimal primal-dual methods for a class of saddle point problems. *SIAM Journal on Optimization*, 24(4), 1779–1814, 2014.

[17] J. Cardelino, V. Caselles, M. Bertalmio, and G. Randall. A contrario selection of optimal partitions for image segmentation. *SIAM Journal on Imaging Sciences*, 6:1274–1317, 2013.

[18] D. Cremers, M. Rousson, and R. Deriche. A review of statistical approaches to level set segmentation: Integrating color, texture, motion and shape. *International Journal of Computer Vision*, 72:195–215, 2007.

[19] I. Ekeland and R. Temam. Convex analysis and variational problems. SIAM, Philadelphia, 1999.

[20] L. C. Evans. Partial differential equations, American Mathematical Society,ISBN 0821807722, 1998.

[21] T. Gevers, A. Gijsenij, J. van de Weijer, and J.-M. Geusebroek. Color in Computer Vision. *Willey*, 2012.

[22] S. Geman and D. Geman. Stochastic relaxation, Gibbs distributions, and the Bayesian restoration of images. *IEEE Transactions on Pattern Analysis and Machine Intelligence* PAMI-6 (1984), pp. 721–741.

[23] T. Goldstein and S. Osher. The split bregman algorithm for l1 regularized problems. *SIAM Journal on Imaging Sciences*, 2:323–343, 2009.

[24] L. Grady. Random Walks for Image Segmentation. *IEEE Transactions on Pattern Analysis and Machine Intelligence*, 28(11):1768–1783, 2006.

[25] L. Grady and C. Alvino. Reformulating and optimizing theMumford-Shah functional on a graph – a faster, lower energy solution. In *European Conference on Computer Vision*, pages 248–261, 2008.

[26] http://www.eecs.berkeley.edu/Research/Projects/CS/vision/bsds.

[27] Y. M. Jung, S. H. Kang, and J. Shen. Multiphase image segmentation via Modica – Mortola phase transition. *SIAM Journal on Applied Mathematics*, 67(5): 1213–1232, 2007

[28] T. Kanungo, D. Mount, N. Netanyahu, C. Piatko, R. Silverman, and A. Wu. An efficient k-means clustering algorithm: analysis and implementation. *IEEE Transactions on Pattern Analysis and Machine Intelligence*, 24:881–892, 2002.

[29] D. Kay and A. Tomasi. Color image segmentation by the vector-valued Allen-Cahn phase-field model: a multigrid solution. *IEEE Transactions on Image Processing*, 18:2330–2339, 2009.

[30] A. Levinshtein, A. Stere, K. Kutulakos, D. Fleet and S. Dickinson. TurboPixels: Fast Superpixels Using Geometric Flows. *IEEE Transactions on Pattern Analysis and Machine Intelligence*, 31(12):2290–2297, 2009.

[31] F. Li, M. Ng, T. Zeng, and C. Shen. A multiphase image segmentation method based on fuzzy region competition. *SIAM Journal on Imaging Sciences*, 3(2):277–299, 2010.

[32] M. Lievin and F. Luthon. Nonlinear color space and spatiotemporal MRF for hierarchical segmentation of face features in video. *IEEE Transactions on Image Processing*, 13(1):63–71, 2004.

[33] L. Macaire, N. Vandenbroucke and J. Postaire. Color image segmentation by pixel classification in an adapted hybrid color space: application to soccer image analysis. *Computer Vision and Image Understanding*, 90(2):190–216, 2003.

[34] D. Mumford and J. Shah. Boundary detection by minimizing functionals. In *Proceedings of IEEE conference on computer vision and pattern recognition*, pages 22–26, 1985.

[35] D. Mumford and J. Shah. Optimal approximations by piecewise smooth functions and associated variational problems. *Communications on Pure and Applied Mathematics*, 42:577–685, 1989.
[36] M. K. Ng, R. H. Chan, and W.-C. Tang. A fast algorithm for deblurring models with Neumann boundary conditions. *SIAM Journal on Scientific Computing*, 21:851–866, 1999.
[37] G. Paschos. Perceptually uniform color spaces for color texture analysis: An empirical evaluation. *IEEE Transactions on Image Processing*, 10(6), pp. 932–937, 2001.
[38] A. Plaza, J. Benediktsson, J. Boardman, *et al.*. Recent advances in techniques for hyperspectral image processing. *Remote Sensing of Environment*, 113(1):110–122, 2009.
[39] T. Pock, D. Cremers, A. Chambolle, and H. Bischof. A convex relaxation approach for computing minimal partitions. In *IEEE Computer Society Conference on Computer Vision and Pattern Recognition (CVPR)*, pages 810–817, 2009.
[40] R. B. Potts. Some generalized order-disorder transformations. *Proceedings of the Cambridge Philosophical Society*, **48**, pp. 106–109, 1952.
[41] C. Rotaru , T. Graf and J. Zhang. Color image segmentation in HSI space for automotive applications. *Journal of Real-Time Image Processing*, 3(4):311–322, 2008.
[42] L. Rudin, S. Osher, and E. Fatemi. Nonlinear total variation based noise removal algorithms. *Physica D*, 60(1):259–268, 1992.
[43] J. Shi and J. Malik. Normalized Cuts and Image Segmentation. *IEEE Transactions on Pattern Analysis and Machine Intelligence*, 22(8):888–905, 2000.
[44] M. Storath and A. Weinmann. Fast partitioning of vector-valued images. *SIAM Journal on Imaging Sciences*, 7(3):1826–1852, 2014.
[45] Y. Tai, J. Jia and C. Tang. Soft Color Segmentation and its Applications *IEEE Transactions on Pattern Analysis and Machine Intelligence*, 29(9):1520–1537, 2007.
[46] D. Townsend. Multimodality imaging of structure and function. *Physics in Medicine and Biology*, 53(4):1–39, 2008.
[47] C. Tai, X. Zhang, and Z. Shen, *Wavelet frame based multiphase image segmentation*, *SIAM Journal on Imaging Sciences*, 6(4), pp. 2521–2546, 2013.
[48] L. Vese and T. Chan. A multiphase level set framework for image segmentation using the Mumford and Shah model. *International Journal of Computer Vision*, 50(3):271–293, 2002.
[49] X. Wang, Y. Tang, S. Masnou and L. Chen. A Global/Local Affinity Graph for Image Segmentation. *IEEE Transactions on Image Processing*, 24(4):1399–1411, 2015.
[50] G. Zhang, J. Jia, W. Hua and H. Bao. Robust Bilayer Segmentation and Motion/Depth Estimation with a Handheld Camera *IEEE Transactions on Pattern Analysis and Machine Intelligence*, 33(3):603–617, 2011.

PLACE PHOTO HERE

Xiaohao Cai received the M.S. degree in mathematics from Zhejiang University, China, in 2008, and the Ph.D. degree in mathematics from The Chinese University of Hong Kong, Hong Kong in 2012.

He is currently a postdoctoral researcher in the Department of Plant Sciences, and Department of Applied Mathematics and Theoretical Physics, University of Cambridge. His research interests include image processing, numerical analysis and their applications in processing of digital image, video, biomedical imaging, remote sensing data, just to name a few.

PLACE PHOTO HERE

Raymond Chan was born in 1958 in Hong Kong. He received his B.Sc. degree in Mathematics from the Chinese University of Hong Kong and his M.Sc. and Ph.D. degree in Applied Mathematics from New York University. He is now a Chair Professor in the Department of Mathematics, The Chinese University of Hong Kong. His research interests include numerical linear algebra and image processing problem.

PLACE
PHOTO
HERE

Mila Nikolova received the Ph.D. degree from the Université de Paris-Sud, France, in 1995.

She got a Habilitation to direct research in 2006. Currently, she is a Research Director with the National Center for Scientific Research (CNRS), Cachan Cedex, France. She performs her duty as a full-time Researcher at the Centre de Mathématiques et de Leurs Applications (CMLA), the 8536 UMR of CNRS, in the Department of Mathematics of ENS de Cachan, France. Her research interests are in mathematical Image and signal reconstruction, inverse problems, regularization and variational methods and the properties of their solutions, and scientific computing.

PLACE
PHOTO
HERE

Tieyong Zeng received the B.S. degree from Peking University, Beijing, China, in 2000, the M.S. degree from Ecole Polytechnique, Paris, France, in 2004, and the Ph.D. degree from the University of Paris XIII, Paris, in 2007. Before joining Hong Kong Baptist University, Kowloon Tong, China, as an Assistant Professor, he was a Post-Doctoral Researcher with the Centre de Mathématiques et de Leurs Applications, ENS de Cachan, Cachan, France. His research interests are image processing, statistical learning, and scientific computing.